

6-1-2023

An improved shallow water temperature model for an Australian tidal wetland environment using publicly available data

Kerry Staples
Edith Cowan University

Steven Richardson
Edith Cowan University

Peter J. Neville
Edith Cowan University

Jacques Oosthuizen
Edith Cowan University

Follow this and additional works at: <https://ro.ecu.edu.au/ecuworks2022-2026>



Part of the [Environmental Sciences Commons](#)

10.3390/w15122221

Staples, K., Richardson, S., Neville, P. J., & Oosthuizen, J. (2023). An improved shallow water temperature model for an Australian tidal wetland environment using publicly available data. *Water*, 15(12), article 2221.

<https://doi.org/10.3390/w15122221>

This Journal Article is posted at Research Online.

<https://ro.ecu.edu.au/ecuworks2022-2026/2718>

Article

An Improved Shallow Water Temperature Model for An Australian Tidal Wetland Environment Using Publicly Available Data

Kerry Staples ^{1,*} , Steven Richardson ² , Peter J. Neville ^{1,3}  and Jacques Oosthuizen ¹ 

¹ Occupational and Environmental Health, School of Medical and Health Sciences, Edith Cowan University, Joondalup, WA 6027, Australia

² Mathematics, School of Science, Edith Cowan University, Joondalup, WA 6027, Australia

³ Biological and Applied Environmental Health, Environmental Health Directorate, Department of Health, Perth, WA 6849, Australia

* Correspondence: k.staples@ecu.edu.au

Abstract: Larval mosquito development is directly impacted by environmental water temperature. Shallow water less than 1 m deep is a common larval mosquito habitat. Existing mathematical models estimate water temperature using meteorological variables, and they range in complexity. We developed a modification of an existing one-layer heat balance model for estimating hourly water temperature and compared its performance with that of a model that uses only air temperature and water volume as inputs and that uses air temperature itself as an indicator of water temperature. These models were assessed against field measurements from a shallow tidal wetland—a known larval habitat—in southwest Western Australia. We also analysed publicly available measurements of air temperature and river height to determine whether they could be used in lieu of field measurements to allow cost-effective long-term monitoring. The average error of the modified version of the heat balance equation was $-0.5\text{ }^{\circ}\text{C}$ per hour. Air temperature was the second-best performing method (\bar{x} error = $-2.82\text{ }^{\circ}\text{C}$). The public data sources accurately represented the onsite water temperature measurements. The original heat balance model, which incorporates a parameterisation of evaporative heat flux, performed poorly in hot, dry, windy conditions. The modified model can be used as an input to larval mosquito development models, assisting Local Government Environmental Health officers to determine optimal mosquito development periods and the timing of mosquito monitoring activities to enhance mosquito control.

Keywords: mathematical modelling; hydrodynamics; water temperature model; shallow waterbody; meteorological data; heat balance; heat flux



Citation: Staples, K.; Richardson, S.; Neville, P.J.; Oosthuizen, J. An Improved Shallow Water Temperature Model for An Australian Tidal Wetland Environment Using Publicly Available Data. *Water* **2023**, *15*, 2221. <https://doi.org/10.3390/w15122221>

Academic Editor: Junhong Bai

Received: 21 April 2023

Revised: 9 June 2023

Accepted: 9 June 2023

Published: 13 June 2023



Copyright: © 2023 by the authors. Licensee MDPI, Basel, Switzerland. This article is an open access article distributed under the terms and conditions of the Creative Commons Attribution (CC BY) license (<https://creativecommons.org/licenses/by/4.0/>).

1. Introduction

The water temperatures of wetlands and shallow water environments affect many biological processes, including the growth of aquatic plants and animals [1]. The role of wetlands as larval mosquito development habitats is important because it can lead to the emergence of vectors of diseases of public health importance, notably the Ross River and Barmah Forest viruses in southwest Western Australia [2–4]. To provide insight into the effects of climate variables on mosquito populations, statistical models have been developed over recent decades. These models link the incidence of these two vector-borne diseases to a range of environmental predictors, notably tides, humidity, rainfall, and air temperature [5–9]. However, statistical models are descriptive rather than explanatory, and do not outline the underlying interactions. To better understand the workings of these relationships, a mechanistic model, built upon the assumed processes, is more valuable. As mosquitoes are poikilotherms, the ability to accurately predict the water temperature of larval mosquito habitats is a necessary foundation for the development of a mechanistic

model of larval growth and development, adult mosquito fecundity, dispersal, and disease transmission dynamics.

Models can only approximate a system. To be useful, a mechanistic model should be easily implemented and sufficiently accurate. In the case of water temperature in a shallow water environment, such as a wetland or pond, a very simple model could approximate water temperature by using the closely correlated air-temperature as a proxy. Daily mean air temperatures have been used to estimate river temperatures in the Lake District of the United Kingdom, providing correlation coefficients of between 0.86 and 0.96 [10]. A water temperature model has been developed for larval mosquito habitats using simple water volume estimates and maximum and minimum air temperatures to estimate water temperature [11]. This was part of a larger model intended to estimate adult mosquito emergence. The model's adult mosquito predictions correlated well with the measured number of adults, but the correlation of the predicted and actual water temperatures was not a part of the study design. The study was conducted in Kilifi, Kenya, a humid area with air temperatures ranging from 20 °C to 37 °C. While very simple, easily implemented, and low cost, this type of model may not capture diurnal temperature variations well enough to model larval development in differing climactic zones.

A more complex heat balance energy budget model which captures instantaneous water temperature more accurately in shallow water environments has subsequently been developed [12]. Capturing hourly fluctuations is important for estimating mosquito larval development as they respond non-linearly to temperature. Mosquitoes have an optimal thermal range within which development increases exponentially. A study conducted in Kisumu, Kenya showed that outside of the upper and lower limits, no, or very limited, development occurs [13]. This water temperature model was further simplified and found to perform well in a similar environment in Kumasi, Ghana, where the water was over 15 cm in depth [14].

The heat balance model requires more complex mathematics and an understanding of the heat balance dynamics of wetlands as it relies on air temperature, humidity, air pressure, wind speed, and water height as measured inputs. The climate in Kisumu, Kenya, is similar to the climate described by Depinay [11], with daily air temperatures ranging from 14 °C to 36 °C and windspeeds below 4 ms⁻¹ over the study period. The heat balance model provided accurate water temperature predictions, but the study was conducted over a relatively short period of time, and the constant water height was calculated using an artificial container with no connection to natural ground water. These limitations mean that the heat balance model requires validation prior to its broad application in natural waterbodies, particularly those with varying depths and in different climates, e.g., with windy and dry, non-humid conditions. The heat balance model utilizes a parametrization of evaporative heat flux, which is the cooling of water due to evaporation. The heat flux parametrization assumes a linear relationship between the energy transfer and the product of wind speed and specific humidity values. However, it has been shown that this assumption does not always hold and requires further testing [15].

There are a number of models for the prediction of temperatures in 3–6 m deep lake environments, and these have been tested simultaneously throughout northern Europe. They have been shown to accurately model water temperature [16,17]. These lake models have been applied predominantly in very cold climates, and in large lakes. The lake models produce multi-layer temperature estimates, but they are also significantly more computationally complex than Paaijmans's parameterized heat balance energy budget model [18–22], and so are likely to be too difficult to be considered for broad use in state and local government mosquito control programs.

Within Australia, a water temperature model has been developed for river systems in southeastern Australia [23], but models for still water bodies less than 1 m deep have not been developed for the Australian environment.

Understanding the processes linking water temperature to larval mosquito development is a vital first step in developing a useful mechanistic model for the entire mosquito

lifecycle. However, increasing model complexity generally means an increase in the number of input variables. Each variable that must be measured increases the cost and time required to develop and maintain the model. Australia has a well-developed network of data collection agencies, including the Bureau of Meteorology and various State Government departments, who routinely collect and make available high quality environmental data, such as tidal observations and river heights and flows. Being able to use these existing data sources would be optimal as a surrogate for the actual physical monitoring of larval mosquito populations.

The purpose of this research was to:

- assess the accuracy of three existing mathematical models for predicting water temperature in natural, shallow water environments of varying depths (0 mm to 600 mm) in an area with hot, dry, windy summers and cool, wet winters, and
- determine whether publicly available datasets can be used in lieu of onsite monitoring equipment for input variable measurement once an initial onsite calibration phase is complete.

2. Materials and Methods

2.1. Study Location

The field study was conducted in the Eastern Swan region of the Perth Metropolitan area at Ashfield Flats in the suburb of Bassendean, Western Australia (Figure 1). The climate in this area is characterized by hot, dry summers, with a mean summer windspeed of 8–10 ms^{-1} , and cool, wet winters [24]. Two tidally driven waterbodies within the Ashfield Flats site were modelled. The surrounding land in this area is predominantly suburban residential land. The ground at the site is flat, varying from 0 mm to 400 mm in height over the main area of interest (Figure 2). Fifteen-minute water height and air temperature measurements for the Ashfield Flats site were obtained from the Department of Biodiversity, Conservation and Attractions for the period August 2018 to November 2020. These measurements formed part of the separate Ashfield Flats Hydrological Study [25]. Initial water temperature measurements, not forming part of the Ashfield Flats Hydrological Study, were recorded by the Department of Biodiversity, Conservation and Attractions, and these were taken at 30-minute intervals with a HOBO S-TMB-M006 temperature sensor (OneTemp Pty Ltd, Adelaide, Australia) from 11 September 2019 to 5 November 2019, a period roughly represent spring, the most active part of the mosquito season. Supplemental measurements were taken by a researcher using a LogTag UTRIX-16 temperature logger (LogTag, Auckland, New Zealand) contained in a waterproof wrapping from 7–11 December 2021 to represent very hot, dry, windy summer conditions.

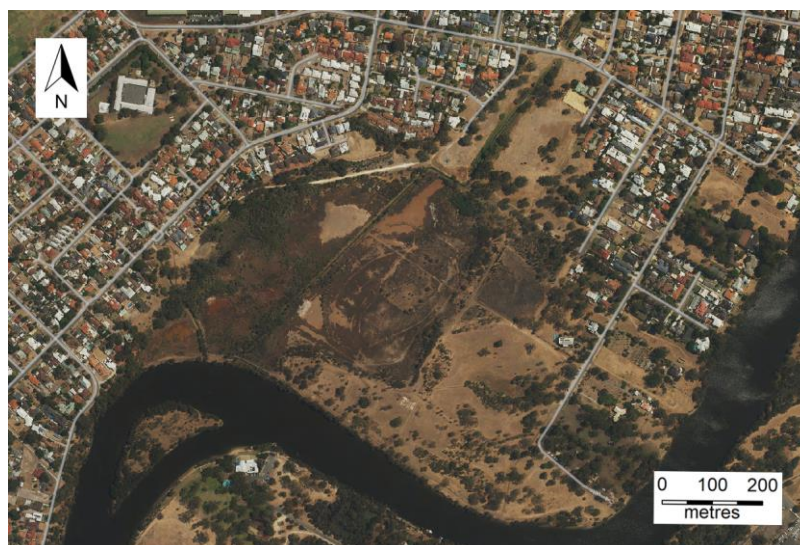


Figure 1. Aerial view of the Ashfield Flats, adjacent to Swan River and bounded by residences [26].

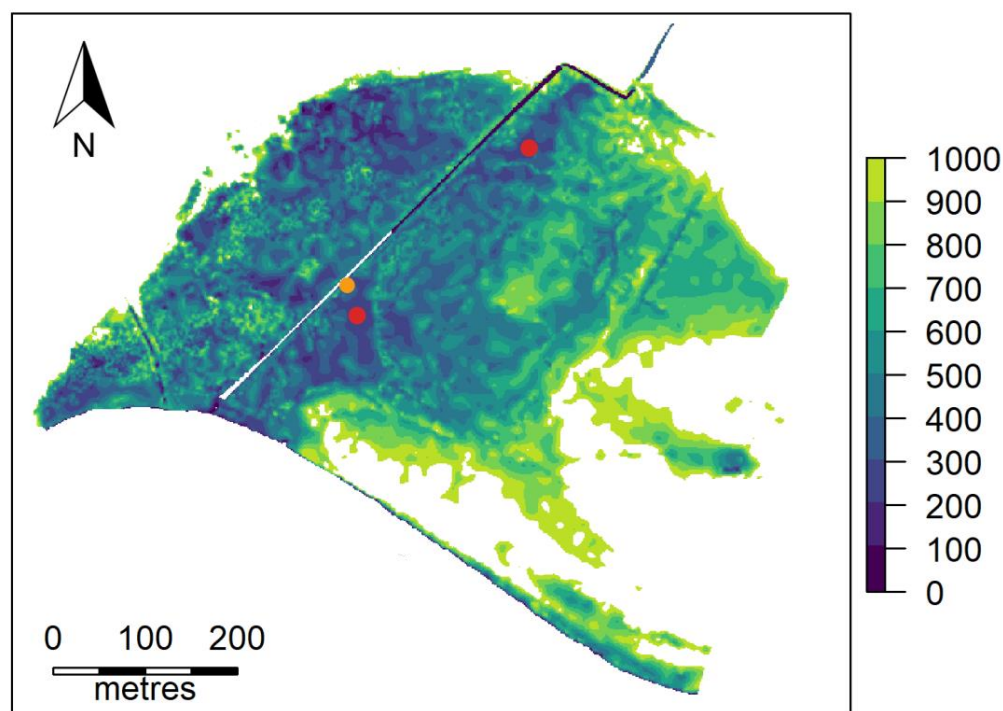


Figure 2. Ashfield Flats site map showing 100 m contour levels, the locations of the two waterbody sampling sites (indicated by the red dots), and the location of the air temperature measurement site (indicated by the orange dot).

2.2. Public Data Sources

Historical tide heights of the Swan River were obtained from a sensor at the Barrack Street Jetty, maintained by the Department of Transport, who monitor river height for ferry movements [27], and these were compared with the peak river height levels recorded by the Meadow Street Bridge sensor [28]. The Barrack Street Jetty is located approximately 8.5 km southwest of the study site. The Meadow Street Bridge is 3.5 km northeast. As the maximum daily river height determines the overflow and inundation of the wetland, the daily maximum heights of the datasets were compared to assess the suitability of the Barrack Street Jetty observations as a proxy for onsite river height (the Barrack Street Jetty data are more easily available and cover a longer historical period).

Weather measurements were obtained from the Bureau of Meteorology [24]. Hourly air temperature data from the closest weather station, Perth Airport, were compared with onsite measurements. The Perth Airport weather station is approximately 2.5 km southeast of the study site. Hourly air pressure, humidity, rainfall, wind-speed, and daily evapotranspiration and pan evaporation data from Perth Airport were also obtained, but these were not cross-validated with onsite measurements.

2.3. Model Description

The model was coded using R Studio Version 2022.02.3 (R version 4.2.0 and the main packages), Matrix v 1.4-1, matrixStats v0.62.0, dplyr v1.0.9, zoo v1.8-10, and lubridate v1.8.0. (RStudio, PBC, Boston, MA, USA).

2.3.1. Water Height Model

The model is as described by Depinay [11], but with the addition of a variable river height component, where W_H is the water height at time, t , in hours, for $i = 1 : n$. The riverbank prevents overflow from the river to the wetland until the river height, R_H , exceeds a minimum river height threshold, R_T (Equation (1), Figure 3). When the river height is below the overflow threshold, water height is determined as the balance of water flowing into and out of the waterbody. Water inflows can be fixed or variable. Fixed inflows,

U_{IF} , include streams, drainage lines, or pipelines that are not considered to change with rainfall. Although there are several drainage lines at this site, they flow past, rather than into the wetland basin and have not been included in the model. Variable inflows are direct rainfall, r_a , and water entering the waterbody due to rainfall runoff. Rainfall runoff, U_{IV} , is an index representing the proportional level of water height increase per 1 mm of rainfall. The site is flat, so rainfall runoff is negligible, and U_{IV} was set equal to one. Water outflows include water lost to soil infiltration, U_O , and water lost due to evapotranspiration, ET . At the site, the ground water table is close to the surface, and water loss due to ground infiltration is negligible. Evapotranspiration can vary considerably from site to site and across vegetation complexes [29]. To account for the specific vegetation evapotranspiration rate at the site, a scale factor, ET_O , selected because it best fit the observed data, was applied to the daily evapotranspiration rate, ET . All water flow variables have units of mmhr^{-1} . The overflow thresholds and ground levels for the ponds were obtained from a previous hydrological study conducted at the site [25].

$$W_H(i + 1) = \begin{cases} R_H & R_H \geq R_T \\ W_H(i) + U_{IF} + U_{IV}r_a - U_O - ET_OET, & R_H < R_T \end{cases} \quad (1)$$

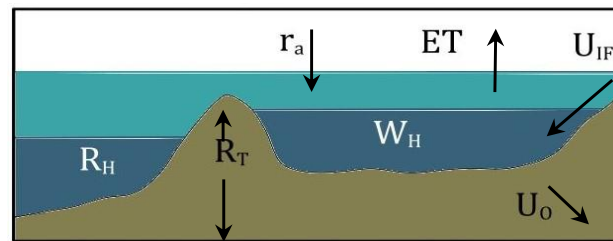


Figure 3. The waterbody height, W_H , is equal to the river height, R_H , when the river height is greater than the riverbank overflow threshold, R_T , as is shown by the light blue area. When the river height, R_H , is lower than the overflow threshold, the waterbody height is determined by rainfall, r_a , soil infiltration, U_O , fixed water inflows, U_{IF} , and evaporation, ET . The direction of the arrows indicated the direction of water flow, except R_T , which indicates the overflow threshold height.

2.3.2. Temperature Models

Three models (Model 1—[11], Model 2—[12], and Model 3—a modified version of [12]) were tested for water temperature and compared with the baseline hourly observed air temperature data used as a proxy for water temperature. These models are described below.

Model 1

This model estimates the proportion of cloud coverage, CC , with values from zero to one, from relative humidity, H (%). Cloud cover is estimated to be zero for H less than 50% and one for H over 95%, increasing linearly between these two points as is shown in Equation (2). Maximum and minimum air temperatures, $T_{a(max)}$ and $T_{a(min)}$, a constant representing the proportion of the waterbody that is unshaded, $U_{SunExpo}$, and the estimated volume of the waterbody, v (L), are used to estimate the maximum water temperature, T_w^M (see Equations (3) and (4)). Water temperature was estimated to be equal to air temperature for water volumes below 10,000 L.

$$CC = \begin{cases} 0, & H \leq 50 \\ \frac{H-50}{45}, & 50 < H < 95 \\ 1, & H \geq 95 \end{cases} \quad (2)$$

$$T_w^M = \begin{cases} T_a, & v \leq 10,000 \\ T_{a(max)} + \Delta T_w^M, & v > 10,000 \end{cases} \quad (3)$$

$$\Delta T_w^M = \begin{cases} \left[\left(\left(\frac{v+1}{100,001} \right)^{0.27} - 2 \right) (1 - CCU_{SunExpo}) - \left(\frac{7(v+1)}{100,001} \right)^{0.43} CCU_{SunExpo} \right], & 10,000 < v \leq 100,000 \\ -1 - 6CCU_{SunExpo}, & v \geq 100,000 \end{cases} \quad (4)$$

Model 2

Changes in water temperature are modelled using a one-layer iterative heat balance equation for shallow water pools (see Equation (5)). Multiple input variables are parameterized, and the only variables requiring measurement are air temperature, air pressure, wind speed, and relative humidity.

$$K_{in}(1 - \alpha_t) + L_{in} + P - L_{out} - H - LE - G_s = \frac{\rho_w c_w W_H(i) \Delta T_w}{\Delta t} \quad (5)$$

The model incorporates incoming shortwave radiation, K_{in} , allowing for solar reflection (albedo), α_t , incoming longwave radiation, L_{in} , outgoing radiation, L_{out} , sensible heat flux, H , evaporation flux, LE , soil heat flux, G_s , advective heat exchange via raindrops, P , the density of water, ρ_w , the specific heat of the water, c_w , the depth of the water pool, W_H , the change in the temperature of the water, ΔT_w , and the change in time, Δt . Advective heat exchange from rain, P , has a minimal effect on water temperature [12], so this term was excluded.

The homogeneous waterbody temperature can be estimated using Equation (5) with respect to the change in water temperature at each time step, as is shown in Equation (6), where $T_w(i + 1) - T_w(i)$ replaces ΔT_w , such that T_w represents the water temperature at the time, t , in hours.

$$T_w(i + 1) = T_w(i) + \frac{\Delta t (K_{in}(1 - \alpha_t) + L_{in} - L_{out} - H - LE - G_s)}{(\rho_w c_w W_H(i))} \quad (6)$$

Equations (7)–(18) describe how each parameter contained in Equation (6) is determined.

The incoming shortwave radiation, K_{in} (Wm^{-2}), is estimated using the proportion of the sky covered by clouds, CC , (see Equation (2)) and the Angot index of incoming radiation, R_o for a specific geographic location [30], which is converted to hourly values [31], as is shown in Equation (7).

$$K_{in}(i) = R_o(0.20 + 0.55(1 - CC(i))) \quad (7)$$

The albedo, α_t , is a measure of solar energy reflectivity at the water surface and can range from zero to one. For clear, shallow water, the overall albedo is determined using a combination of the albedo of the bottom of the pool (0.06 to 0.08 [30]) and the fraction of shortwave radiation absorbed at the pool surface, and it has been estimated to have a value of 0.15 in this type of environment [11]. The albedo of water surfaces with high solar elevation has been estimated to range from 0.03 to 0.1 [32], so a lower albedo of 0.1 was also tested. We used the parameter value that gave the best fit of the resulting model to the observed data, minimized the mean hourly difference between the model and the observed water temperatures, and used a combination of root mean square error (RMSE) and the sum of the cumulative hourly errors.

The incoming longwave radiation, L_{in} (Wm^{-2}), is modelled as a function of ambient air temperature, T_a ($^{\circ}C$), water vapour pressure, e (hPa), a cloud height factor, d , and the Stephan Boltzmann constant, σ , as is shown in Equation (8).

$$L_{in}(i) = \left[0.56 + 0.067 \sqrt{e(i) \sigma T_a(i)^4} + d(i) C(i) \right] \quad (8)$$

The cloud height factor, d , is assigned a value ranging from 30 (low cloud) to 60 (high cloud) and increases linearly between these values, as is shown in Equation (9). Low clouds

are those at an altitude of 2 km or less; high clouds are those at an altitude of 6 km or greater [33].

$$d(i) = \begin{cases} 30, & h(i) \leq 2 \\ 7.5h(i) + 15, & 2 < h(i) < 6 \\ 60, & 6 \leq h(i) \end{cases} \quad (9)$$

The cloud height, h , is calculated using the difference between the air temperature, T_a ($^{\circ}\text{C}$), and the dew point temperature, DP ($^{\circ}\text{C}$), multiplied by a conversion factor, which gives a height in kilometres [34], as is shown in Equation (10).

$$h(i) = 0.122(T_a(i) - DP(i)) \quad (10)$$

The dew point temperature, DP ($^{\circ}\text{C}$), can be determined using the water vapour pressure, e (hPa), as is shown in Equation (11) [35].

$$DP(i) = \frac{116.91 + 237.3 \ln(e(i))}{16.78 - \ln(e(i))} \quad (11)$$

The water vapour pressure, e (hPa), can be calculated using the relative humidity, RH (%), and the ambient air temperature, T_a ($^{\circ}\text{C}$), as is shown in Equation (12) [12].

$$e(i) = RH(i) \left[611.2 \exp\left(\frac{17.67T_a(i)}{T_a(i) + 243.5}\right) \right] \quad (12)$$

The outgoing longwave radiation, L_{out} (Wm^{-2}), is a product of the emissivity of the water, ε_w (0.98), the Stephan Boltzmann constant, σ , and the water temperature, $T_w(i)$, as is shown in Equation (13) [12].

$$L_{out}(i) = \varepsilon_w \sigma (T_w(i) + 273)^4 \quad (13)$$

The sensible heat flux, H (Wm^{-2}), is the heat exchange via convection at the water surface, and it is determined using the density of air, ρ_a (kgm^{-3}), the heat capacity of air, c_p ($\text{Jkg}^{-1} \text{K}^{-1}$), the wind speed at 2.0 m above ground, u (ms^{-1}), the heat transfer coefficient, C_h , and the air temperature, T_a ($^{\circ}\text{C}$), as is shown in Equation (14).

$$H(i) = \rho_a c_p u(i) C_h (T_w(i) - T_a(i)) \quad (14)$$

The evaporation flux, LE (Wm^{-2}), is the heat exchange via evaporation at the water surface, and it is modelled using the latent heat for vaporization, λ (Jkg^{-1}), the wind speed, u (ms^{-1}), the heat transfer coefficient, C_h , the saturation-specific humidity at the water surface, q_w (kgkg^{-1}), and the specific humidity at the reference height, q_a (kgkg^{-1}), as is shown in Equation (15) [12].

$$LE(i) = \rho_a \lambda(i) u(i) C_h (q_w(i) - q_a(i)) \quad (15)$$

The specific humidity of the air, q_a (kgkg^{-1}), can be calculated using the water vapour pressure, e (hPa), and the atmospheric pressure, p (hPa), as is shown in Equation (16) [35], with e as given by Equation (13).

$$q_a(i) = \frac{0.622e(i)}{p - 0.378e(i)} \quad (16)$$

The specific humidity at the water surface, q_w (kgkg^{-1}), can also be determined using Equation (16) by substituting the saturated water vapour pressure over the water, e_w (hPa),

in place of e . The saturation vapour pressure over the water is calculated using the air temperature, T_a ($^{\circ}\text{C}$), as is shown in Equation (17).

$$e_w(i) = 0.61078 \exp\left(\frac{17.27T_a(i)}{T_a(i) + 237.3}\right) \quad (17)$$

The soil heat flux, G_s (Wm^{-2}), is the heat conduction at the soil/water interface, and it is estimated using the net solar radiation, as is shown in Equation (18) [12].

$$G_s(i) = 0.15 (K_{in}(i) (1 - \alpha) + L_{in}(i) - L_{out}(i)) \quad (18)$$

Model 3

Model 3 is a modified version of Model 2 in which the evaporation flux, LE , is replaced with an alternative evaporation flux, LE_a (Wm^{-2}), which is calculated using the observed pan evaporation, E_p (mmday^{-1}). Pan evaporation is converted using a pan evaporation coefficient, $E_{po}(i)$, and a scale factor, $E_{ps}(i)$, as is shown in Equation (19). When compared with natural waterbodies, an evaporation pan overestimates evaporation due to additional heating through the sides of the evaporation pan. To account for this, a pan evaporation coefficient, E_{po} , is applied using the equation for a Class A evaporation pan with a dry fetch [36]. Pan evaporation measurements are only available as daily figures, so this gives a daily total for evaporative heat flux. To maintain the hourly distribution the proportion of heat flux transferred each hour, E_{ps} is determined by dividing the hourly LE by the total daily LE , as is shown in Equation (20). This alternative value for evaporative heat flux, LE_a , is used in Equation (6), and all other variables are as described for Model 2.

$$LE_a(i) = E_{po}(i)E_p(i)E_{ps}(i) \quad (19)$$

$$E_{ps}(i) = \frac{LE(i)}{\sum_1^{24} LE(i)} \quad (20)$$

3. Results

3.1. Public Data Source Validation

3.1.1. Air Temperature

A comparison of the hourly air temperatures at Perth Airport and the onsite measurements for the period from 11 September to 5 November 2019 is shown in Figure 4a. Most of the observations at the airport were within ± 2 $^{\circ}\text{C}$ of the onsite measurements, and the differences are approximately normally distributed, with a mean of -0.12 $^{\circ}\text{C}$ and a standard deviation 1.20 $^{\circ}\text{C}$, as is shown in Figure 4b.

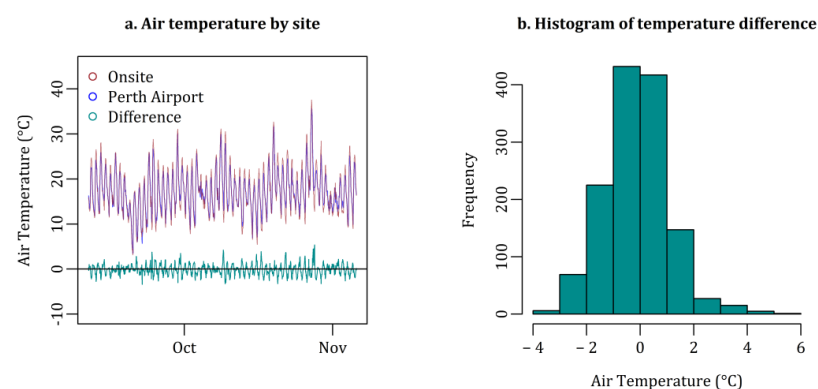


Figure 4. (a) Air temperature measured onsite and at Perth Airport, the closest permanent weather station (2.5 km from the study site) from 11 September to 5 November 2019. The green line shows the difference between the two site measurements. (b) A histogram of the differences between the hourly measured air temperatures at Perth Airport and those at Ashfield Flats.

3.1.2. River Height

Figure 5a shows the measured water heights at the Barrack Street Jetty and the Meadow Street Bridge from 1 January to 13 February 2019. During this period, the Meadow Street Bridge mean river height 0.747 m above that of the Barrack Street Jetty. This difference was added to the Barrack Street Jetty observations, and both were compared, as is shown in Figure 5b. The differences are approximately normally distributed, with a standard deviation of 0.033 m.

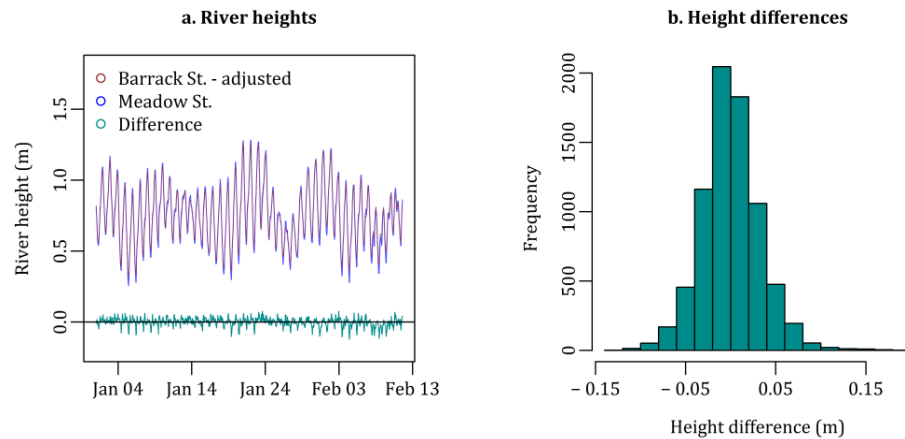


Figure 5. (a) Hourly river heights from 1 January to 13 February 2019 for the Meadow Street Bridge and the Barrack Street Jetty. The green line shows the difference between the measured and predicted observations. (b) A histogram of the hourly river height differences between the Barrack Street Jetty and the Meadow Street Bridge.

3.2. Water Depth

The water height model output was compared with the river heights observed between 1 January 2019 to 11 November 2019. The measured and predicted water depths and tidal peaks are shown in Figure 6. An equipment fault in pond 1 meant that only the pond 2 water heights were available for comparison. The model for pond 2 shows a good correlation with the measured water levels. Peak tidal heights and subsequent overflow into the waterbody are also well predicted by the model. The evapotranspiration coefficient, ET_0 , used in Equation (1), was set to 2 by selecting the coefficient that resulted in the waterbody drying out in the model at the same time as in the observed data.

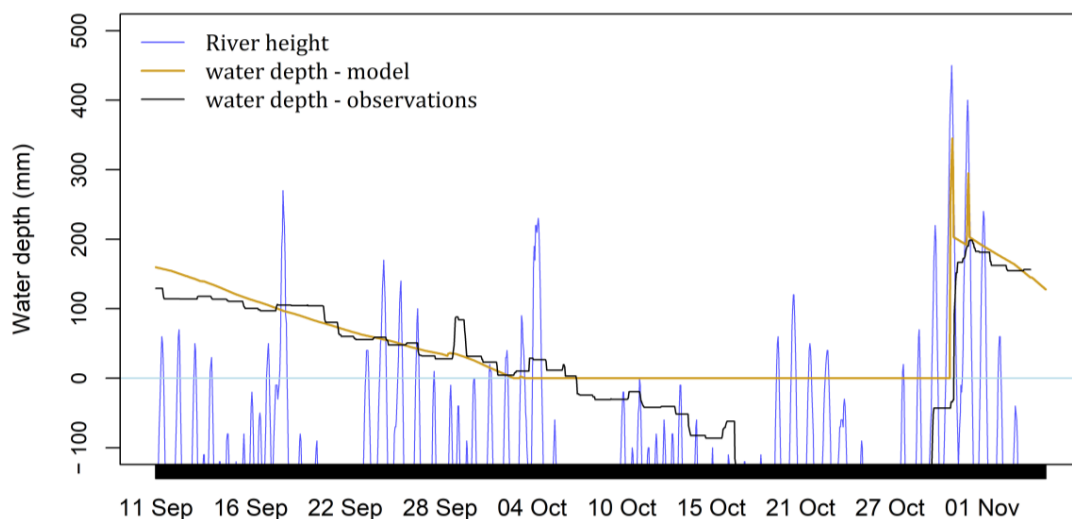


Figure 6. Observed river tide heights and modelled and observed pond water depths from 11 September 2019 to 5 November 2019. A water depth of zero indicates that there is no standing water left in the pond.

3.3. Water Temperature

The output for the three temperature models was compared with the onsite measurements for the period 11 September to 5 November 2019. The results are shown in Figure 7. A subset of the output during which the water depth decreased from 71 mm to 0 mm is shown in Figure 8.

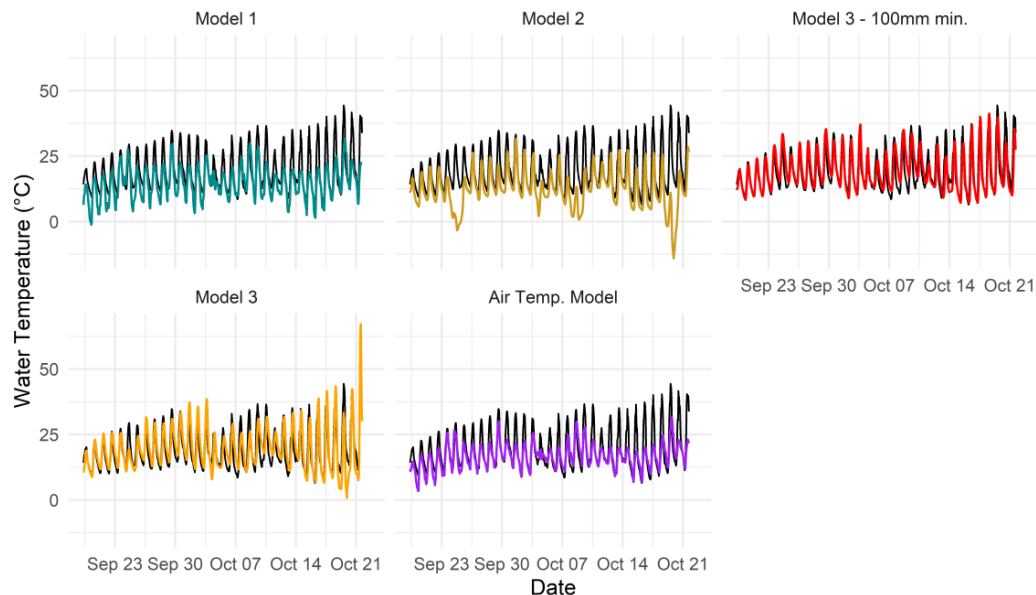


Figure 7. Modelled and measured water temperatures for Model 1 (blue), Model 2 (yellow), Model 3 (100 mm minimum water depth) (red), Model 3 (no minimum water depth) (orange), and the Air Temperature Model (purple) from 11 September to 5 November 2019. Measured temperatures are shown in black.

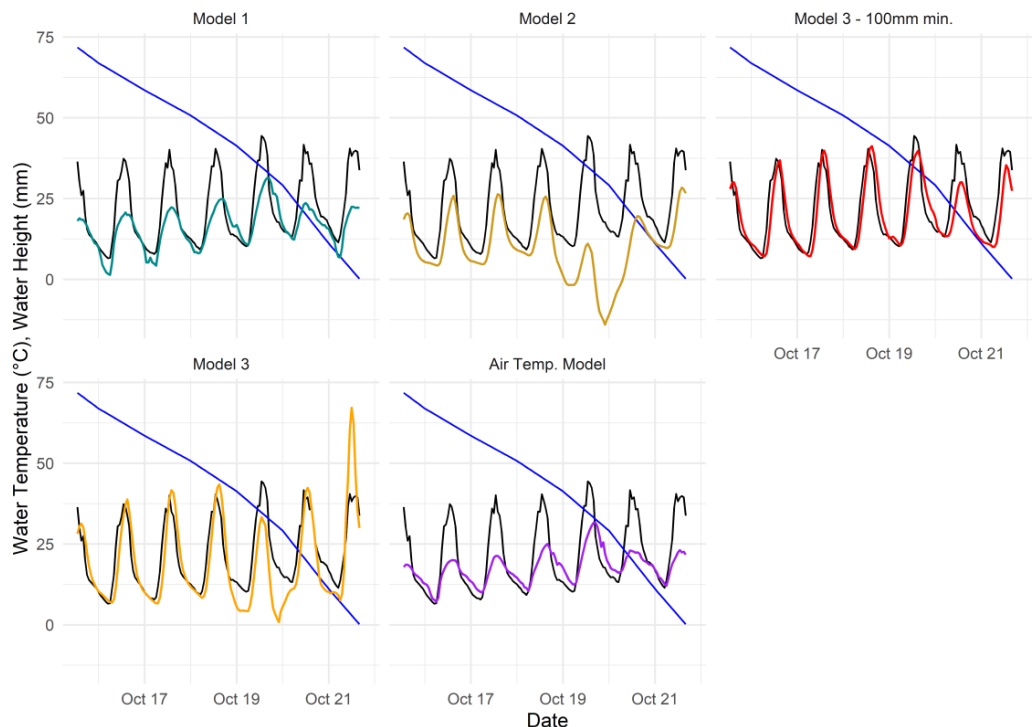


Figure 8. Subset of modelled and measured water temperatures for Model 1 (blue), Model 2 (yellow), Model 3 (3 (100 mm minimum water depth) (red), Model 3 (no minimum water depth) (orange), and the Air Temperature Model (purple) from 15 to 23 October 2019. Measured temperatures are shown in black; water depth is shown in blue.

Model 1 has no parameters set by estimation, but Models 2 and 3 contain estimated variables that were trained using data from this period. Models 2 and 3 were initially implemented as described above, but the output showed increasing temperature variations as water depth decreased from September to October 2018. To limit this, a minimum water depth of 100 mm was introduced, (i.e., the water height W_H , calculated in Equation (1) was replaced by 100 mm where $W_H(i) < 100$ mm). The result of this change is shown in Figures 6 and 7 (Model 3 with 100 mm minimum (red) and Model 3 with no minimum (orange)). In Model 2, it was also necessary to decrease the windspeed by 50 percent in Equations (15) and (16) to obtain a reasonable model fit. Once this adjustment was applied, albedo values of 0.1 and 0.15 were tested for Models 2 and 3. The value minimising both the root mean square error (RMSE) and the sum of the cumulative hourly errors was selected, and this was α_t equal to 0.1 for Model 2 and α_t equal to 0.15 for Model 3.

Once parameter estimation was finalized, the output from Models 1 and 2, Model 3 with the 100 mm minimum water depth, and the Air Temperature Model were compared with the measured water temperatures for the five-day period 7–11 December 2021, as is shown in Figure 8. The results obtained using the parametrized evaporative heat flux, LE , in Model 2 and the pan evaporation-derived evaporative heat flux, LE_a , in Model 3 are shown along with the measured and modelled water temperatures in Figure 8. The RMSE and mean cumulative error of each model for both time periods, along with the error obtained by using air temperature as a proxy for water temperature, are shown in Table 1.

Table 1. Root mean square errors and cumulative mean errors between modelled and observed hourly water temperatures (°C).

Model	Spring		Summer		Overall	
	RMSE	\bar{x}	RMSE	\bar{x}	RMSE	\bar{x}
Model 1	5.46	−4.95	4.91	−1.66	5.41	−4.69
Model 2	6.78	−6.59	32.29	−32.29	8.80	−8.62
Model 3	3.68	−0.65	2.05	1.27	3.55	−0.50
Air Temperature	4.11	−3.01	4.30	−0.64	4.12	−2.82

The mean hourly difference in temperature for each measurement period and the overall differences are shown in Table 1, along with the mean error obtained using air temperature directly as a proxy for water temperature.

4. Discussion

The ability to accurately estimate both the daily mean water temperature and the daily maximum and minimum temperatures is important because, within species-specific optimal temperature ranges, mosquito larvae develop more quickly at higher temperatures, and when within the upper and lower bounds of their preferred temperature window, their development is exponential rather than linear [13]. This means that even one hour spent at a higher temperature can lead to faster larval development, while an hour spent outside of their optimal temperature range may reduce the larvae's development and lead to higher mortality or slower development.

Overall, all of the models underestimated the water temperature to some extent. This result is consistent with the water temperature results of the lake model [16]. When compared using air temperature alone as a proxy for water temperature, Model 3 was more accurate in the spring in terms of mean hourly differences and RMSE. In the summer, Model 3 had a higher mean difference but a lower RMSE, and overall it performs better than air temperature alone. Importantly, only Model 3 estimates daily maximum temperatures well, as is shown in Figures 6 and 7.

Model 2, which is the heat balance system with a parameterized evaporative heat flux, became significantly inaccurate in these conditions, predicting water temperatures

well below freezing. High wind speed and low humidity in the parameterized heat flux correlate with freezing water temperatures, and the difference in the magnitude of the two heat fluxes correlates well with the large variation in the temperature predictions between Models 2 and 3 (Figure 9).

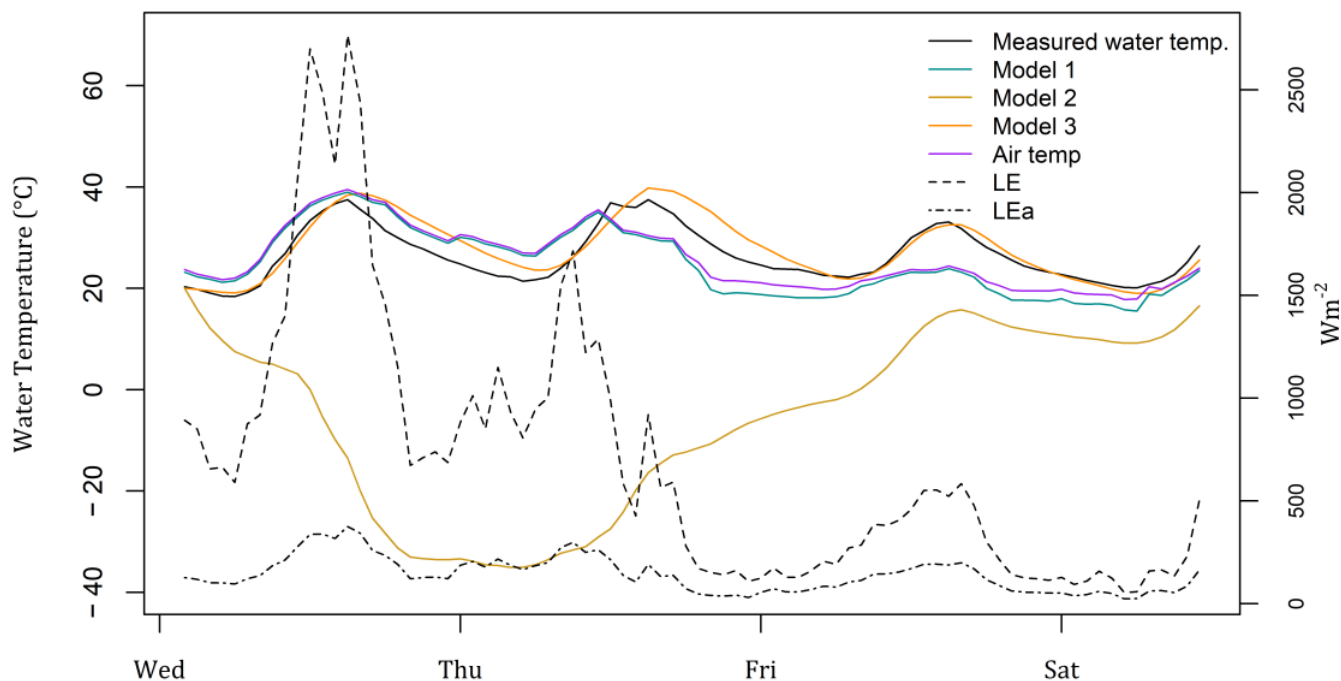


Figure 9. Models for summer temperatures vs. alternative evaporative heat flux, LE_a , and parameterized evaporative heat flux, LE , from 8 to 11 December 2022.

It was also necessary to reduce the spring windspeed by 50% to obtain a good approximation of water temperature. This suggests that the heat flux parameterization is overly sensitive when applied to areas with higher wind speeds. This agrees with the findings of Zhang and Liu [15], who observed that the association between specific humidity, windspeed, and heat flux is non-linear. Given this inaccuracy in areas subject to high windspeed and low humidity, the direct measurement of heat flux may be considered, but this would not completely overcome this issue due to the energy balance closure problem, a full discussion of which is outside of the scope of this paper [37,38]. The alternative estimation of evaporative heat flux derived from pan evaporation measurements provides a more accurate estimate in these weather conditions, expanding the range of climates in which Model 2 [12] can be applied when modified as described (Model 3).

Model 3, when the 100 mm minimum water depth constraint was applied, remained consistent with the actual values, approximating the diurnal temperature fluctuations accurately, and it outperformed the other models with a cumulative mean error within 1 °C of the measured values over both measurement periods. Surprisingly, using air temperature as a proxy for water temperature enabled it to outperform both Model 1 and Model 2, showing that more complex equations do not always provide better results.

A minimum water depth was needed for the heat balance models to avoid large temperature fluctuations at low water depths. The original study by Paaijmans [12] was conducted in plastic-lined containers of constant depth rather than in natural waterbodies with underlying saturated soil or in contact with groundwater. The present study was conducted in an area with a significant underlying groundwater table, and this may function as a temperature buffer, minimizing the more extreme temperature losses and gains. A simplified version of the heat balance model used in Kumasi, Ghana (and in equatorial Africa) also found poor model performance at water depths less than 15 cm [14].

This would need to be explored in further studies. However, the addition of a minimum water level to the model reduced the impact of this variable on the model's performance.

When considering the ability of the model to accurately predict the maximum and minimum water temperatures, Model 3, the modified heat balance model, was significantly more accurate than using air temperature or Model 1. Model 1 underestimated both the maximum and the minimum daily water temperatures and did not provide any advantage over using air temperature alone to predict daily minimum water temperatures (Figure 8). In the context of mosquito biology, lower temperatures do not impact mortality rates as much as higher temperatures, so accuracy in predicting maximum water temperatures is prioritized over the accurate prediction of minimum temperatures. Model 1 provided slightly improved maximum temperature prediction and improved overall mean temperature prediction, so its use over air temperature alone can be justified. However, the modified heat balance model significantly outperformed both air temperature and Depinay's model.

The combination of Depinay's water depth model [11] and Model 3 (Paaijmans's temperature model [12] with the alternative heat flux component) gives a good approximation of the expected water depth, the timing of wetland inundation, the mean water temperature, and the daily extreme water temperatures. In terms of hourly water temperature predictions, Model 3 offers an overall improvement over using the air temperature or Models 1 or 2, particularly in hot, dry, windy conditions.

Although using this model necessitated an initial period of onsite measurement and calibration, there is justification for using this more complex model over air temperature alone as it provides more accurate hourly water temperature predictions in the temperate climate of southwest Western Australia. Once an initial calibration period has been conducted in the field, ongoing onsite measurement can be replaced with the use of publicly available data for air temperature and river height, reducing ongoing maintenance costs.

As was outlined in the Introduction, a number of water temperature models have been developed for use in lakes, including the Flake, CLM4-LISSS, LAKE, SimStrat, and LAKEoneD models [18–22]. All of these produce estimates of the change in water temperature with water depth, including the surface water temperature of a lake. Mathematical complexity aside, any of these models could be used to model water temperatures in shallow wetlands. The performance of these lake models was evaluated using a long-term water temperature dataset for two lakes in Northern Europe [16,17]. All five models were shown to accurately model surface water temperature, with mean RMSEs of 1–2.2 °C, and the FLake model has since been optimized for use in a series of 94 large lakes in China, with the reported RMSE remaining at around 2 °C [39]. These RMSE values are similar to the summer RMSE—and lower than the overall RMSE—of the simpler modified heat balance model developed in this study. The higher RMSE in this study may be due to the very shallow depth of the wetland area under study, which has a maximum depth of 0.4 m and is frequently 0.2 m or less. When water is shallow, and especially as it tends towards completely drying out, there is a lower thermal mass available per meter squared of water surface area to absorb heat energy, resulting in larger daily temperature fluctuations when compared with deeper water. This could cause errors to be magnified and impact the overall RMSE. Lake models have been more commonly conducted in lakes with mean depths of 2 m or greater. These lake models tend to have been developed to model climate or weather patterns, or to model pollutants or gaseous concentrations, rather than the growth and development of poikilothermic organisms, and as such, the accuracy of maximum and minimum diurnal water temperature predictions is not discussed, and so cannot be compared with the results of the current study.

At the other end of the spectrum from a mechanistic model is the rapidly evolving area of machine learning, which has been used to model water temperature in lakes in Minnesota and Wisconsin in the United States [40]. The machine learning model gave results with a mean RMSE of 1.65 °C for a series of 68 lakes, results similar to those produced by the lake models. The fidelity of the model to daily maximum and minimum temperatures was not recorded. The aim of this research is to develop a mechanistic model

with explanatory power; machine learning algorithms are not able explain their results, and so are not considered further here.

Within Australia, the state and local governments are responsible for the prevention of mosquito-borne disease, and they accomplish this predominantly through larval mosquito reduction programs [41,42]. The physical monitoring of larval habitats is time-consuming, but it is considered the most effective monitoring method [43]. Reducing the frequency of site visits would reduce strain on limited government resources. The water temperature model developed from this research has been used as an input to a linked larval mosquito development model used to predict populations of mosquito vectors of Ross River virus [44], and this in turn can be used by mosquito control program managers in southwest Western Australia to assist in identifying the times larvae are most likely to be developing in numbers large enough to warrant larvicidal treatment. This water temperature model will also be used to examine how mosquito populations may change under different climate change scenarios, enabling planning for the expansion or reduction of future mosquito control programs and assisting with town planning decisions for housing developments adjacent to identified mosquito habitat hotspots. Future research could also couple this model with remote sensing data which can measure water depth in similar wetlands to provide mosquito population predictions to local mosquito managers.

This study was limited by the relatively short period during which onsite measurements were taken, and it should be replicated using longer-term monitoring. However, the river height gauges and Perth Airport weather station are close to the site, providing accurate proxies for onsite environmental measurements, so the input data are robust. A second limitation is the generalizability of the model to other geographic locations. The model has been calibrated to the specific conditions found in southwest Western Australia, i.e., hot, dry, windy summers in a shallow tidal wetland, and close scrutiny of assumptions and testing of model specifications and performance is required prior to deployment in new geographies.

5. Conclusions

In this study, we have developed an improved water height and heat balance water temperature model capable of capturing hourly water temperatures, including accurate approximations of daily maximum and minimum water temperatures, in very shallow wetland sites in southwest Western Australia. The model performs better than simpler methods of approximating water temperature. The model gives an RMSE comparable with those of more mathematically complex lake models in summer, but it has higher RMSE values in winter and overall, and it has an overall cumulative error of -0.5 °C. This study was conducted in a known larval habitat of non-uniform depth, so it is a significant step forward in the application of a theoretical water temperature model to a real-world environment and will be of use in the development of mechanistic mosquito development models for use by state and local governments in mosquito control programs.

Author Contributions: Conceptualization, K.S.; methodology, K.S. and S.R.; software, K.S.; validation, K.S. and S.R.; formal analysis, K.S.; investigation, K.S.; resources, K.S., P.J.N., and J.O.; data curation, K.S.; writing—original draft preparation, K.S.; writing—review and editing, K.S., S.R., P.J.N., and J.O.; visualization, K.S.; supervision, S.R., P.J.N., and J.O.; project administration, K.S.; funding acquisition, J.O. All authors have read and agreed to the published version of the manuscript.

Funding: This research received no external funding.

Institutional Review Board Statement: Not applicable.

Informed Consent Statement: Not applicable.

Data Availability Statement: Publicly available datasets were analyzed in this study. Tide height data were obtained from the Department of Transport and are available from <https://www.transport.wa.gov.au/imate/download-tide-wave-data.asp> (accessed on 19 November 2021). River height data were obtained from the Department of Transport and are available from <https://www.transport.wa.gov.au/imate/download-tide-wave-data.asp> (accessed on 19 November 2021). Restrictions apply to the availability of the weather data, which were obtained from the Bureau of Meteorology and are available from <http://www.bom.gov.au/climate/data-services/data-requests.shtml> (accessed on 21 November 2021) with the permission of the Bureau of Meteorology. Restrictions apply to the availability of the water height and air temperature measurements for the Ashfield Flats site, which were obtained from the Research Hydrologist, Ecosystems Science, Department of Biodiversity and Conservation. An R code is available from the corresponding author on request. All remaining relevant data are included within the paper.

Acknowledgments: The Department of Biodiversity, Conservation and Attractions provided technical advice and access to water height monitoring equipment.

Conflicts of Interest: The authors declare no conflict of interest.

References

- Jacobs, A.F.G.; Heusinkveld, B.G.; Kraai, A.; Paaijmans, K.P. Diurnal Temperature Fluctuations in an Artificial Small Shallow Water Body. *Int. J. Biometeorol.* **2008**, *52*, 271–280. [[CrossRef](#)] [[PubMed](#)]
- Lindsay, M.; Johansen, C.; Broom, A.K.; Smith, D.W.; Mackenzie, J.S. Emergence of Barmah Forest Virus in Western Australia. *Emerg. Infect. Dis.* **1995**, *1*, 22–26. [[CrossRef](#)]
- Kerridge, P. *Aspects of the Ecology and Biology of the Salt-Marsh Mosquito Aedes Vigilax (Skuse)*; University of Queensland: Brisbane, Australia, 1971.
- Kay, B.H.; Sinclair, P.; Marks, E.N. Mosquitoes: Their Interrelationship with Man. In *The Ecology of Pests—Some Australian Case Histories*; Kitching, R.L., Jones, R.E., Eds.; CSIRO: Canberra, Australia, 1981; pp. 157–174.
- Hu, W.; Nicholls, N.; Lindsay, M.; Dale, P.; McMichael, A.J.; Mackenzie, J.S.; Tong, S. Development of a Predictive Model for Ross River Virus Disease in Brisbane, Australia. *Am. J. Trop. Med. Hyg.* **2004**, *71*, 129–137. [[CrossRef](#)]
- Kokkinn, M.J.; Duval, D.J.; Williams, C.R. Modelling the Ecology of the Coastal Mosquitoes *Aedes Vigilax* and *Aedes Camporhynchus* at Port Pirie, South Australia. *Med. Vet. Entomol.* **2009**, *23*, 85–91. [[CrossRef](#)] [[PubMed](#)]
- Koolhof, I.S.; Bettiol, S.; Carver, S. Fine-Temporal Forecasting of Outbreak Probability and Severity: Ross River Virus in Western Australia. *Epidemiol. Infect.* **2017**, *145*, 2949–2960. [[CrossRef](#)]
- Williams, C.R.; Fricker, S.R.; Kokkinn, M.J. Environmental and Entomological Factors Determining Ross River Virus Activity in the River Murray Valley of South Australia. *Aust. N. Z. J. Public Health* **2009**, *33*, 284–288. [[CrossRef](#)] [[PubMed](#)]
- Woodruff, R.E.; Guest, C.S.; Garner, M.G. Summarising the Mosquito: Genetic Parameters for Prediction of Arbovirus Epidemics. *Arbovirus Res. Aust.* **2000**, *8*, 420–422.
- Crisp, D.T.; Howson, G. Effect of Air Temperature upon Mean Water Temperature in Streams in the North Pennines and English Lake District. *Freshw. Biol.* **1982**, *12*, 359–367. [[CrossRef](#)]
- Depinay, J.-M.O.; Mbogo, C.M.; Killeen, G.; Knols, B.; Beier, J.; Carlson, J.; Dushoff, J.; Billingsley, P.; Mwambi, H.; Githure, J.; et al. A Simulation Model of African Anopheles Ecology and Population Dynamics for the Analysis of Malaria Transmission. *Malar. J.* **2004**, *3*, 29. [[CrossRef](#)]
- Paaijmans, K.P.; Heusinkveld, B.G.; Jacobs, A.F.G. A Simplified Model to Predict Diurnal Water Temperature Dynamics in a Shallow Tropical Water Pool. *Int. J. Biometeorol.* **2008**, *52*, 797–803. [[CrossRef](#)]
- Sharpe, P.J.H.; DeMichele, D.W. Reaction Kinetics of Poikilotherm Development. *J. Theor. Biol.* **1977**, *64*, 649–670. [[CrossRef](#)] [[PubMed](#)]
- Asare, E.O.; Tompkins, A.M.; Amekudzi, L.K.; Ermert, V.; Redl, R. Mosquito Breeding Site Water Temperature Observations and Simulations towards Improved Vector-Borne Disease Models for Africa. *Geospat. Health* **2016**, *11*, 391. [[CrossRef](#)]
- Zhang, Q.; Liu, H. Seasonal Changes in Physical Processes Controlling Evaporation over Inland Water: Seasonal Changes in Lake Evaporation. *J. Geophys. Res. Atmos.* **2014**, *119*, 9779–9792. [[CrossRef](#)]
- Stepanenko, V.; Jöhnk, K.D.; Machulskaya, E.; Perroud, M.; Subin, Z.; Nordbo, A.; Mammarella, I.; Mironov, D. Simulation of Surface Energy Fluxes and Stratification of a Small Boreal Lake by a Set of One-Dimensional Models. *Tellus Dyn. Meteorol. Oceanogr.* **2014**, *66*, 21389. [[CrossRef](#)]
- Stepanenko, V.M.; Martynov, A.; Jöhnk, K.D.; Subin, Z.M.; Perroud, M.; Fang, X.; Beyrich, F.; Mironov, D.; Goyette, S. A One-Dimensional Model Intercomparison Study of Thermal Regime of a Shallow, Turbid Midlatitude Lake. *Geosci. Model Dev.* **2013**, *6*, 1337–1352. [[CrossRef](#)]
- Mironov, D.V. *Parameterization of Lakes in Numerical Weather Prediction Description of a Lake Model*; COSMO; Deutscher Wetterdienst: Offenbach am Main, Germany, 2008.
- Hostetler, S.W.; Bartlein, P.J. Simulation of Lake Evaporation with Application to Modeling Lake Level Variations of Harney-Malheur Lake, Oregon. *Water Resour. Res.* **1990**, *26*, 2603–2612. [[CrossRef](#)]

20. Stepanenko, V.M.; Machul'skaya, E.E.; Glagolev, M.V.; Lykossov, V.N. Numerical Modeling of Methane Emissions from Lakes in the Permafrost Zone. *Izv. Atmos. Ocean. Phys.* **2011**, *47*, 252–264. [[CrossRef](#)]
21. Goudsmit, G.-H.; Burchard, H.; Peeters, F.; Wüest, A. Application of K- ϵ Turbulence Models to Enclosed Basins: The Role of Internal Seiches: Application of K- ϵ Turbulence Models. *J. Geophys. Res. Ocean.* **2002**, *107*, 23-1–23-13. [[CrossRef](#)]
22. Joehnk, K.D.; Umlauf, L. Modelling the Metalimnetic Oxygen Minimum in a Medium Sized Alpine Lake. *Ecol. Model.* **2001**, *136*, 67–80. [[CrossRef](#)]
23. Joehnk, K.D.; Graham, K.; Sengupta, A.; Chen, Y.; Aryal, S.K.; Merrin, L.; Durr, P.A. The Role of Water Temperature Modelling in the Development of a Release Strategy for Cyprinid Herpesvirus 3 (CyHV-3) for Common Carp Control in Southeastern Australia. *Water* **2020**, *12*, 3217. [[CrossRef](#)]
24. Bureau of Meteorology Climate Data Online 2021. Available online: <http://www.bom.gov.au/climate/data/index.shtml> (accessed on 26 November 2021).
25. Department Biodiversity, Conservation and Attractions. *Ashfield Flats Hydrological Study*; Department Biodiversity, Conservation and Attractions: Kensington, Australia, 2021.
26. Town of Bassendean Town of Bassendean Online Mapping System n.d. Available online: <http://tob.office-on-the.net:50080/intramaps80/> (accessed on 21 November 2019).
27. Department of Transport Historical Tide and Wave Data—Barrack Street Jetty 2021. Available online: <https://www.transport.wa.gov.au/imagery/download-tide-wave-data.asp> (accessed on 19 November 2021).
28. Department of Water Water Information Reporting 2019. Available online: <http://wir.water.wa.gov.au/Pages/Water-Information-Reporting.aspx> (accessed on 19 November 2019).
29. Mohamed, Y.A.; Bastiaanssen, W.G.M.; Savenije, H.H.G.; van den Hurk, B.J.J.M.; Finlayson, C.M. Wetland versus Open Water Evaporation: An Analysis and Literature Review. *Phys. Chem. Earth Parts ABC* **2012**, *47–48*, 114–121. [[CrossRef](#)]
30. Stull, R. Wet-Bulb Temperature from Relative Humidity and Air Temperature. *J. Appl. Meteorol. Climatol.* **2011**, *50*, 2267–2269. [[CrossRef](#)]
31. Collares-Pereira, M.; Rabl, A. The Average Distribution of Solar Radiation—Correlations between Diffuse and Hemispherical and between Daily and Hourly Insolation Values. *Sol. Energy* **1979**, *22*, 155–164. [[CrossRef](#)]
32. Sumner, G.N. *Precipitation: Process and Analysis*; Wiley: Chichester, UK; New York, NY, USA, 1988; ISBN 978-0-471-90534-9.
33. Met Office. *Cloud Types for Observers: Reading the Sky*; Met Office: Exeter, UK, 2006.
34. United States; Federal Aviation Administration. *Pilot's Handbook of Aeronautical Knowledge 2016*; Aviation Supplies and Academics Inc.: New Castle, DE, USA, 2016; ISBN 978-1-61954-477-2.
35. Jensen, M.E.; Allen, R.G.; American Society of Civil Engineers; Environmental and Water Resources Institute (U.S.) (Eds.) *Evaporation, Evapotranspiration, and Irrigation Water Requirements*, 2nd ed.; ASCE Manuals and Reports on Engineering Practice; American Society of Civil Engineers: Reston, VA, USA, 2016; ISBN 978-0-7844-1405-7.
36. Food and Agriculture Organization of the United Nations. *Crop Evapotranspiration: Guidelines for Computing Crop Water Requirements*; Allen, R.G., Ed.; FAO Irrigation and Drainage Paper; Food and Agriculture Organization of the United Nations: Rome, Italy, 1998; ISBN 978-92-5-104219-9.
37. Foken, T. The Energy Balance Closure Problem: An Overview. *Ecol. Appl.* **2008**, *18*, 1351–1367. [[CrossRef](#)]
38. Jin, Y.; Liu, Y.; Liu, J.; Zhang, X. Energy Balance Closure Problem over a Tropical Seasonal Rainforest in Xishuangbanna, Southwest China: Role of Latent Heat Flux. *Water* **2022**, *14*, 395. [[CrossRef](#)]
39. Huang, L.; Wang, X.; Sang, Y.; Tang, S.; Jin, L.; Yang, H.; Ottlé, C.; Bernus, A.; Wang, S.; Wang, C.; et al. Optimizing Lake Surface Water Temperature Simulations Over Large Lakes in China with FLake Model. *Earth Space Sci.* **2021**, *8*, e2021EA001737. [[CrossRef](#)]
40. Read, J.S.; Jia, X.; Willard, J.; Appling, A.P.; Zwart, J.A.; Oliver, S.K.; Karpatne, A.; Hansen, G.J.A.; Hanson, P.C.; Watkins, W.; et al. Process-Guided Deep Learning Predictions of Lake Water Temperature. *Water Resour. Res.* **2019**, *55*, 9173–9190. [[CrossRef](#)]
41. Tomerini, D.M. The Impact of Local Government Mosquito Control Programs on Ross River Virus Disease in Queensland, Australia. Ph.D. Thesis, Griffith University, Queensland, Australia, 2008.
42. Tomerini, D.M.; Dale, P.E.; Sipe, N. Does Mosquito Control Have an Effect on Mosquito-Borne Disease? The Case of Ross River Virus Disease and Mosquito Management in Queensland, Australia. *J. Am. Mosq. Control Assoc.* **2011**, *27*, 39–44. [[CrossRef](#)]
43. Silver, J.B.; Service, M.W. *Mosquito Ecology: Field Sampling Methods*; Springer: Dordrecht, The Netherlands, 2008; ISBN 978-1-4020-6666-5.
44. Staples, K.; Richardson, S.; Neville, P.J.; Oosthuizen, J. A Multi-Species Simulation of Mosquito Disease Vector Development in Temperate Australian Tidal Wetlands Using Publicly Available Data. *Trop. Med. Infect. Dis.* **2023**, *8*, 215. [[CrossRef](#)]

Disclaimer/Publisher's Note: The statements, opinions and data contained in all publications are solely those of the individual author(s) and contributor(s) and not of MDPI and/or the editor(s). MDPI and/or the editor(s) disclaim responsibility for any injury to people or property resulting from any ideas, methods, instructions or products referred to in the content.